Data-Driven Quantitative Multiobjective Finite-Control-Set Model Predictive Control for Three-Phase Three-Level NPC Inverters

Xu Zhang, Zhixun Ma, *Senior Member, IEEE*, Haichuan Niu, *Student Member, IEEE*, Xiang Wu, *Member, IEEE*, Xinbo Cai, and Guobin Lin

***Abstract*—This article presents a data-driven quantitative multiobjective finite-control-set model predictive control (FCS-MPC) for three-phase three-level neutral point clamped (NPC) inverters, aiming to achieve precise control of both the switching frequency and the neutral point voltage. Considering the switching weighting factor and the neutral point voltage weighting factor as inputs, and the average switching frequency within a fixed sliding window time and the maximum value of the neutral point voltage within another fixed sliding window time as outputs, a compact form dynamic linearization (CFDL) method is employed to construct an equivalent dynamic linearized data model at each dynamic operating point of the closed-loop system. Building upon this data-driven model, a meticulously crafted controller is devised to precisely regulate both the switching frequency and the peak deviation of the neutral-point potential. The simulation and experimental results validate the correctness and demonstrate the superiority of the proposed control approach.**

***Index Terms*—Data-driven, finite-control-set (FCS), model predictive control (MPC), neutral point voltage control, switching frequency control, three-level inverter, three-phase inverter.**

I. Introduction

With the advancement of digital signal processor technology, model predictive control has garnered increasing attention in the field of power electronics [1], [2], [3], [4]. Finite-control-set model predictive control (FCS-MPC) is widely studied for its strengths in multiobjective optimization and nonlinear control [5], [6], [7]. Its short discrete period compared to the switching period enhances low-frequency precision and avoids narrow pulses, making it highly suitable for controlling low switching frequency, high-power converters [8], [9], [10].

Received 17 June 2025; revised 9 September 2025 and 13 November 2025; accepted 11 December 2025. Date of publication 16 December 2025; date of current version 20 March 2026. This work was supported in part by the National Natural Science Foundation of China under Grant 52372359 and in part by China Postdoctoral Science Foundation under Grant 2022M712397. Recommended for publication by Associate Editor D. D. C. Lu. *(Corresponding author: Zhixun Ma.)*

Xu Zhang, Zhixun Ma, Haichuan Niu, Xiang Wu, and Guobin Lin are with the College of Transportation, Tongji University, Shanghai 201804, China (e-mail: lnyk_zhangxu@tongji.edu.cn; zhixun.ma@tongji.edu.cn; 2311634@tongji.edu.cn; wux@cumt.edu.cn; 12154@tongji.edu.cn).

Xinbo Cai is with Shanghai STEP Electric Corporation, Shanghai 201802, China (e-mail: xinbo.cai@tum.de).

Color versions of one or more figures in this article are available at https://doi.org/10.1109/TPEL.2025.3644891.

Digital Object Identifier 10.1109/TPEL.2025.3644891

FCS-MPC can easily realize multiobjective optimization; however, it is difficult to obtain a clear relationship between its weighting factors and optimization targets [11]. The coupling of multiple optimization objectives often necessitates extensive offline tuning of weighting factors [12], [13], [14], [15], [16], [17]. Fixed weighting factors degrade performance once the operating point shifts. Offline parameter tuning methods are inadequate for achieving ideal multiobjective optimization across different operating points.

In [18], a neural network model was employed to map the relationship between the switching frequency weighting factor and the switching frequency under various operating conditions, thereby enabling online adjustment of the weighting factor. Machado et al. [19] utilized a neural network model to fit the switching frequency, neutral point potential, current tracking error, and current total harmonic distortion (THD) under different operating conditions, realizing a dynamic multiweighting approach. The neural network approach necessitates offline training, and each alteration to the controlled object or parameters requires retraining. Moreover, the neural network fitting method lacks systematic feedback during online operation, leading to potential issues with model generalization. Liu et al. [20] implemented a self-adjusting technique for weighting factors. However, it independently adjusts multiple weighting factors, neglecting the coupling effects between multiple control objectives and without verifying the applicability of quantitative multiobjective control. To address the challenge of controlling nonlinear systems with unknown models, an adaptive data-driven control method utilizing online data was proposed in [21]. This method exhibited satisfactory performance in regulating the average switching frequency of single-phase three-level neutral point clamped (NPC) rectifiers. However, the approach in [21] was restricted to the online tuning of a single weighting factor, which consequently enabled the quantitative control of only a single objective.

This article presents a quantitative multiobjective control approach that continuously reshapes its own weighting factors online. The principal contributions are threefold.

1) Closed-loop, quantitative regulation of multiple performance indices is attained in real time through data-driven weight adaptation, bypassing any offline training stage.
2) The scheme operates without knowledge of the system model or parameters.

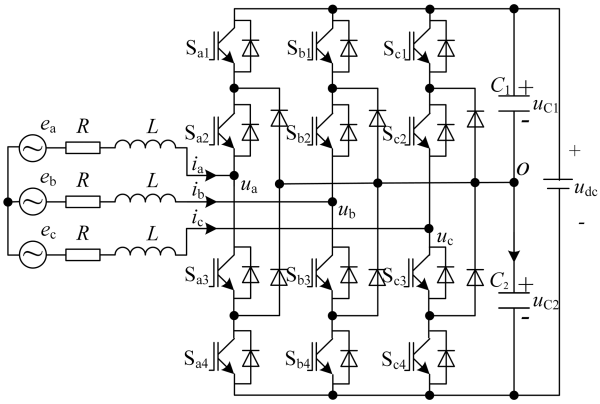

Fig. 1 Three-phase three-level NPC inverter topology.

TABLE I
SWITCHING STATE

Gate signals (S_{x1}, S_{x2})	Output voltage (u_{xo})	Switching state (s_x)
(1,1)	$u_{dc}/2$	1
(0,1)	0	0
(0,0)	$-u_{dc}/2$	-1

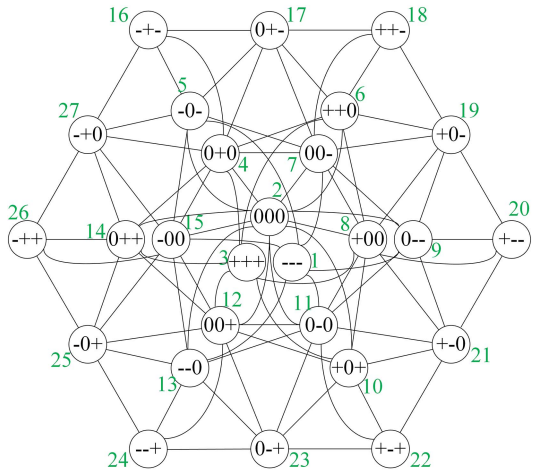

Fig. 2 Switching states of a three-phase three-level inverter.

3) The same framework readily extends to any power-electronic topology or optimization goal within the FCS-MPC family.

II. Finite-Control-Set Model Predictive Control of Three-Phase Three-Level NPC Inverter

The circuit diagram is shown in Fig. 1. The three-level NPC produces three valid switching states in each branch, where $S_x \in \{-1, 0, 1\}$. Assuming the voltage of each capacitor is equal to half of the dc-link voltage, these three switching states produce an output voltage (relative to point o shown in Fig. 1) of $u_{xo} \in \{u_{dc}/2, 0, -u_{dc}/2\}$. Table I summarizes the switching states produced by this inverter. The power inverter generates a total of $3^3 = 27$ switching states, as depicted in Fig. 2.

The voltage equation of the converter in the static $\alpha\beta$ coordinate system is given by

$$L\frac{\mathrm{d}\boldsymbol{i}_{\alpha\beta}}{\mathrm{d}t} = \boldsymbol{e}_{\alpha\beta} - R\boldsymbol{i}_{\alpha\beta} - \boldsymbol{u}_{\alpha\beta} \tag{1}$$

where $\boldsymbol{i}_{\alpha\beta}$ is the $\alpha\beta$ grid side current, $\boldsymbol{e}_{\alpha\beta}$ is the $\alpha\beta$ grid voltage, $\boldsymbol{u}_{\alpha\beta}$ is the output $\alpha\beta$ axis voltage on the ac side of the inverter, L and R are the inductance value of the filter inductor and its equivalent resistance, respectively. The $\alpha\beta$ coordinate system variables can be obtained using the Clarke transform $\boldsymbol{T}_{\alpha\beta}$. $\boldsymbol{i}_{\alpha\beta} = \boldsymbol{T}_{\alpha\beta}\,\boldsymbol{i}_{abc}$, $\boldsymbol{e}_{\alpha\beta} = \boldsymbol{T}_{\alpha\beta}\,\boldsymbol{e}_{\mathrm{abc}}$, $\boldsymbol{u}_{\alpha\beta} = \boldsymbol{T}_{\alpha\beta}\,\boldsymbol{u}_{\mathrm{abc}}$, $\boldsymbol{i}_{\mathrm{abc}} = [i_{\mathrm{a}}, i_{\mathrm{b}}, i_{\mathrm{c}}]^{\mathrm{T}}$, $\boldsymbol{e}_{\mathrm{abc}} = [e_{\mathrm{a}}, e_{\mathrm{b}}, e_{\mathrm{c}}]^{\mathrm{T}}$, $\boldsymbol{u}_{\mathrm{abc}} = [u_{\mathrm{ao}}, u_{\mathrm{bo}}, u_{\mathrm{co}}]^{\mathrm{T}}$

$$\boldsymbol{T}_{\alpha\beta} = \frac{2}{3}\begin{bmatrix} 1 & -\frac{1}{2} & -\frac{1}{2} \\ 0 & \frac{\sqrt{3}}{2} & -\frac{\sqrt{3}}{2} \end{bmatrix}. \tag{2}$$

Equation (1) can be written as the following discrete form:

$$\boldsymbol{i}_{\alpha\beta}^{\mathrm{k}+1} = \left(1 - \frac{T_{\mathrm{s}}R}{L}\right)\boldsymbol{i}_{\alpha\beta}^{\mathrm{k}} + \frac{T_{\mathrm{s}}}{L}\left(\boldsymbol{e}_{\alpha\beta}^{\mathrm{k}} - \boldsymbol{u}_{\alpha\beta}^{\mathrm{k}}\right) \tag{3}$$

where T_{s} is the sampling period, $\boldsymbol{i}_{\alpha\beta}^{\mathrm{k}}$ is the current on the grid side of the $\alpha\beta$ axis at time k, $\boldsymbol{e}_{\alpha\beta}^{\mathrm{k}}$ is the grid voltage of the $\alpha\beta$ axis at time k, $\boldsymbol{u}_{\alpha\beta}^{\mathrm{k}}$ is the output voltage of the ac side of the $\alpha\beta$ axis rectifier at time k.

In formula (3), $\boldsymbol{u}_{\alpha\beta}^{\mathrm{k}}$ can be calculated from the current dc bus voltage $u_{\mathrm{dc}}^{\mathrm{k}}$ and the switching states $s_{\mathrm{a}}^{\mathrm{k}}$, $s_{\mathrm{b}}^{\mathrm{k}}$, $s_{\mathrm{c}}^{\mathrm{k}}$ at time k

$$\boldsymbol{u}_{\alpha\beta}^{\mathrm{k}} = u_{\mathrm{dc}}^{\mathrm{k}}\boldsymbol{T}_{\alpha\beta}\boldsymbol{s}_{\mathrm{abc}}^{\mathrm{k}}. \tag{4}$$

The rate of change of the current, as derived from (1) and (4), is influenced by system parameters, grid voltage, the output voltage on the ac side, and the instantaneous current value. The control system regulates the current by adjusting the ON/OFF states and durations of the switching devices in the inverter, thereby modifying the output voltage on the ac side.

The $\alpha\beta$ grid side voltage at time k+1 can be expressed as follows:

$$\boldsymbol{e}_{\alpha\beta}^{\mathrm{k}+1} = \boldsymbol{e}_{\alpha\beta}^{\mathrm{k}} \cdot e^{j2\pi\omega T_s}. \tag{5}$$

The predicted value of grid-side voltage active and reactive power at time k+1 is

$$\begin{bmatrix} p^{k+1} \\ q^{k+1} \end{bmatrix} = \frac{3}{2}\begin{bmatrix} e_\alpha^{k+1} & e_\beta^{k+1} \\ -e_\beta^{k+1} & -e_\alpha^{k+1} \end{bmatrix}\begin{bmatrix} i_\alpha^{k+1} \\ i_\beta^{k+1} \end{bmatrix}. \tag{6}$$

The neutral-point potential is defined as

$$u_o^k = u_{C1}^k - u_{C2}^k. \tag{7}$$

The predicted value of neutral-point potential at time k+1 is

$$u_o^{k+1} = u_o^k + \frac{T_s}{C}\sum_{x=a,b,c}\left|s_x^k\right| i_x^k. \tag{8}$$

The switching rule diagram for the three-level inverter is shown in Fig. 2. The future values of the grid-side current $\boldsymbol{i}_{\alpha\beta}^{\mathrm{k}+1}$, grid-side voltages $\boldsymbol{e}_{\alpha\beta}^{\mathrm{k}+1}$, active power $p^{\mathrm{k}+1}$, reactive power $q^{\mathrm{k}+1}$, and neutral-point potential $u_{\mathrm{o}}^{\mathrm{k}+1}$ are predicted for the candidate switching states generated by the inverter using (3), (5), (6), and

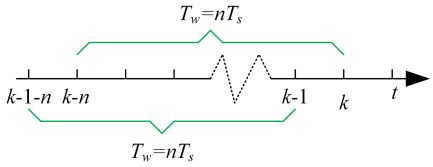

Fig. 3 Schematic diagram of average switching frequency calculation.

(8). The switching state that minimizes the cost function (9) is selected and applied in the next control cycle [22], [23]

$$J=\left(p^{k+1}-p_{\text{ref}}\right)^2+\left(q^{k+1}-q_{\text{ref}}\right)^2+w_o\left(u_o^{k+1}\right)^2+w_n(n_c)^2. \tag{9}$$

Here, w_o and w_n are the weighting factors for neutral point voltage and switching frequency, respectively, and n_c is the number of switching.

III. Quantitative Calculation Method for Switching Frequency and Midpoint Potential

To enable quantitative control of the optimization objectives, they must first be made measurable. Here, the objectives are defined as the average switching frequency and the peak deviation of the neutral-point potential, each evaluated within its own fixed-length sliding window. The following section details how these two metrics are computed online.

A. Quantitative Calculation of Switching Frequency

The average switching frequency was computed within a predefined time observation window, as reported in [21].

The schematic of the calculation method for average switching frequency is shown in Fig. 3. The number of switching times within the observation window is summed up. At each sampling time, the last element n_c^{k-n} of the sum is removed and replaced with the current element *nk c*

$$\Sigma^k=\Sigma^{k-1}+n_c^k-n_c^{k-n} \tag{10}$$

where $n=T_w/T_s$, where T_w is the length of the sliding window time and T_s is the sampling time. Σ represents the total number of n_c during the time T_w. The mathematical relationship between the average switching frequency f_{sw} over the sliding window time T_w and Σ is given as follows:

$$f_{\text{sw}}=\frac{\Sigma^k}{12T_w}. \tag{11}$$

In this article, T_w is set to 20 ms. The integer 12 denotes the 12 insulated gate bipolar transistors (IGBTs) within the NPC inverter. The value of f_{sw} at time t represents the average switching frequency during time (t-T_w, t).

B. Quantitative Calculation of Neutral-Point Potential

In a three-level NPC converter, the neutral-point potential drifts slowly, so a long sliding window (T_{lw}) is required to capture its peak excursion. To avoid storing the entire dataset, we propose a sequential comparator that tracks the running maximum of the absolute value in real time; the idea is sketched in Fig. 4 and detailed below.

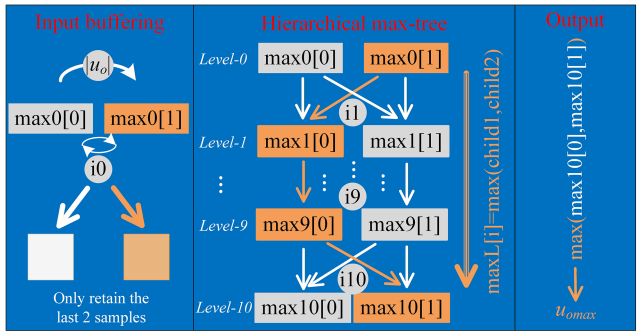

Fig. 4 Principle of maximum value extraction in fixed sliding time window.

1). Input Buffering: Each new sample $|u_0|$ is written into a rotating 2-element buffer max0. A persistent index i0 toggles between 0 and 1, so only the last two values are retained.

2). Hierarchical Max-Tree: The algorithm builds a binary tree of maxima in place. Pairs from one level (e.g., max1[0] and max1[1]) are compared and the larger is promoted to the next level (max2[i2]). Indices i1, i2, i3 cycle 0→1→0, giving fully sequential, allocation-free operation.

3). Output: When the tree is complete, the root value $u_{o\max}$—the largest sample in the current window—is delivered immediately.

IV. Sliding Window Weighting Factor Approach

The sliding window weighting factor approach can achieve control of the average switching frequency, and a fixed switching frequency weighting can accurately track different reference values of switching frequency [21], [26]. On this basis, by dynamically adjusting only the neutral-point potential weighting factor, control of both the neutral-point potential and the average switching frequency can be realized. The control flowchart is shown in Fig. 5.

The value function of the sliding window weighting factor method is given by

$$J=\left(p^{k+1}-p_{\text{ref}}\right)^2+\left(q^{k+1}-q_{\text{ref}}\right)^2+w_{so}^{k+1}\left(u_o^{k+1}\right)^2 +w_{sn}\left(f_{\text{sw}}^{k+1}-f_{\text{sw\_ref}}^{k+1}\right)^2. \tag{12}$$

The neutral-point potential weighting factor *wk*+1 *so*is defined as

$$w_{so}^{k+1}=w_{so}^k+\xi_{so}\frac{u_{o\ \max\ \text{\_ref}}-u_{o\max}^k}{u_{o\max\_\text{ref}}+u_{o\max}^k} \tag{13}$$

where ξ_{so} denotes the step-size factor for the neutral-point potential weighting.

The sliding window weighting factor method exhibits steady-state error [21], [26]. To compensate for this steady-state error, the reference of switching frequency is dynamically adjusted

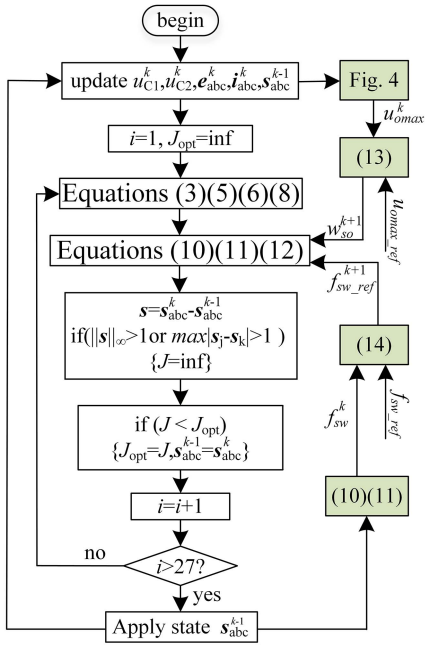

Fig. 5 Principle of sliding window weighting factor approach.

and updated as

$$f^{k+1}_{sw\_\mathrm{ref}} = f^k_{sw\_\mathrm{ref}} + \xi_{sw}\frac{f_{sw\_\mathrm{ref}} - f^k_{sw}}{f_{sw\_\mathrm{ref}} + f^k_{sw}} \tag{14}$$

where ξ_{sw} represents the step-size factor for the switching frequency.

V. Data-Driven Multiobjective Quantitative Control Approach

In this article, the FCS-MPC is employed to dynamically adjust the switching frequency weighting factor w_n and the neutral-point potential weighting factor w_o, based on the average switching frequency within a fixed sliding time window and the peak deviation of the neutral-point potential within a fixed sliding time window.

The multi-input–multioutput (MIMO) system, which takes the weighting factors w_n and w_o as inputs and the average switching frequency f_{sw} and the peak deviation of the neutral-point potential within a fixed sliding time window u_o as outputs, employs a data-driven control approach to achieve precise control of the average switching frequency and t the peak deviation of the neutral-point potential.

A. Dynamic Linearization Method for Discrete-Time Nonlinear Systems

The MIMO nonlinear system considered in this work can be described as follows:

$$\boldsymbol{y}^{k+1} = f\left(\boldsymbol{y}^k, \boldsymbol{y}^{k-1}, \cdots, \boldsymbol{y}^{k-n_y}, \boldsymbol{u}^k, \boldsymbol{u}^{k-1}, \cdots, \boldsymbol{u}^{k-n_u}\right) \tag{15}$$

where $\boldsymbol{u}^k = [w^k_n, w^k_o]^{\mathrm{T}} \in \boldsymbol{R}^2$ and $\boldsymbol{y}^k = [f^k_{sw}, u^k_{omax}]^{\mathrm{T}} \in \boldsymbol{R}^2$ respectively represent the input and output of the system at time k. n_y and n_u are two unknown positive integers. $f(\cdots) = (f_1(\cdots), f_2(\cdots), \cdots, f_{\mathrm{m}}(\cdots))^{\mathrm{T}} \in \prod_{n_y+n_u+2} \boldsymbol{R}^2$ is an unknown nonlinear function.

To simplify the description, let $\Delta\boldsymbol{y}^{k+1} = \boldsymbol{y}^{k+1}$-$\boldsymbol{y}^k$ be the output changes at two neighboring moments, and $\Delta\boldsymbol{u}^{k+1} = \boldsymbol{u}^{k+1}$-$\boldsymbol{u}^k$ be the input changes at two neighboring moments. For the nonlinear system (15), there must be a time-varying parameter $\boldsymbol{\Phi}^k \in \boldsymbol{R}^{2\times 2}$ called pseudoJacobian matrix (PJM), so that the system (15) can be transformed into a data model (16) and $\boldsymbol{\Phi}^k$ is bounded at any time k [24], [25]

$$\Delta\boldsymbol{y}^{k+1} = \boldsymbol{\Phi}^k \Delta\boldsymbol{u}^k \tag{16}$$

where $\boldsymbol{\Phi}^k = \begin{bmatrix} \phi^k_{11} & \phi^k_{12} \\ \phi^k_{21} & \phi^k_{22} \end{bmatrix} \in \boldsymbol{R}^{2\times 2}$ represents the PJM of the system.

The dynamic characteristics of PJM may be very complex and difficult to be described mathematically, but its numerical behavior may be simple and easy to estimate. PJM is just a mathematical concept. The existence of PJM is strictly proved in theory [24], [25].

B. Control Algorithm

Consider the following control input criterion function:

$$J\left(\boldsymbol{u}^k\right) = \|\boldsymbol{y}^{k+1}_{\mathrm{ref}} - \boldsymbol{y}^{k+1}\|^2 + \lambda\|\boldsymbol{u}^k - \boldsymbol{u}^{k-1}\|^2 \tag{17}$$

where $\lambda > 0$ is a weighting factor used to penalize excessive changes in the control input. $\boldsymbol{y}^{k+1}_{ref}$ is the reference value.

To enhance the generalizability of the algorithm, a step-size factor $\rho \in (01]$ is incorporated. By substituting (16) into the criterion function (17), differentiating with respect to $\boldsymbol{u}$, and equating the derivative to zero, the following result is derived:

$$\boldsymbol{u}^k = \boldsymbol{u}^{k-1} + \rho\left(\lambda\boldsymbol{I} + \left(\boldsymbol{\Phi}^k\right)^T\boldsymbol{\Phi}^k\right)^{-1}\left(\boldsymbol{\Phi}^k\right)^T\left(\boldsymbol{y}^{k+1}_{\mathrm{ref}} - \boldsymbol{y}^k\right). \tag{18}$$

In (18), the parameter λ constrains the variation of the control input $\boldsymbol{u}$. This constraint is employed to ensure that the control signal exhibits a requisite degree of smoothness in the control system design.

C. PJM Estimation Algorithm

The PJM estimation criterion function is

$$J\left(\boldsymbol{\Phi}^k\right) = \|\Delta\boldsymbol{y}^k - \boldsymbol{\Phi}^k\Delta\boldsymbol{u}^{k-1}\|^2 + \mu\|\boldsymbol{\Phi}^k - \hat{\boldsymbol{\Phi}}^{k-1}\|^2 \tag{19}$$

where $\mu > 0$ is a weighting factor, employed to penalize excessive variations in the estimated PJM.

To enhance the flexibility and generality of the algorithm, a step-size factor $\eta \in (02]$ is introduced. By minimizing the criterion function (19), the following projection algorithm is obtained:

$$\begin{aligned}\hat{\boldsymbol{\Phi}}^k = \; & \hat{\boldsymbol{\Phi}}^{k-1} + \eta\left(\Delta\boldsymbol{y}^k - \hat{\boldsymbol{\Phi}}^{k-1}\Delta\boldsymbol{u}^{k-1}\right)\left(\Delta\boldsymbol{u}^{k-1}\right)^T \\ & \times\left(\mu\boldsymbol{I} + \Delta\boldsymbol{u}^{k-1}\left(\Delta\boldsymbol{u}^{k-1}\right)^T\right)^{-1}.\end{aligned} \tag{20}$$

The $\hat{\boldsymbol{\Phi}}^k = \begin{bmatrix} \hat{\phi}_{11}^k & \hat{\phi}_{12}^k \\ \hat{\phi}_{21}^k & \hat{\phi}_{22}^k \end{bmatrix} \in \boldsymbol{R}^{2\times 2}$ is the estimate of the PJM. The parameter η represents the search step size of PJM, which characterizes the search speed of PJM.

D. Control Strategy

Based on the PJM estimation algorithm (20) and control algorithm (18), the data-driven quantitative multiobjective control strategy can be given as follows:

$$\begin{cases} \hat{\phi}_{ii}^k = \hat{\phi}_{ii}^1, \left|\hat{\phi}_{ii}^k\right| < b_1 \text{ or } \left|\hat{\phi}_{ii}^k\right| > \alpha b_1 \text{ orsign } \left(\hat{\phi}_{ii}^k\right) \\ \quad \neq \text{sign}\left(\hat{\phi}_{ii}^1\right), i = 1, 2 \\ \hat{\phi}_{ij}^k = \hat{\phi}_{ij}^1, \left|\hat{\phi}_{ij}^k\right| > b_2 \text{ or sign } \left(\hat{\phi}_{ij}^k\right) \\ \quad \neq \text{sign}\left(\hat{\phi}_{ij}^1\right), i, j = 1, 2, i \neq j \\ \hat{\boldsymbol{\Phi}}^k = \hat{\boldsymbol{\Phi}}^{k-1} + \eta\left(\Delta \boldsymbol{y}^k - \hat{\boldsymbol{\Phi}}^{k-1}\Delta \boldsymbol{u}^{k-1}\right)\left(\Delta \boldsymbol{u}^{k-1}\right)^T, \text{ else} \\ \quad \times\left(\mu \boldsymbol{I} + \Delta \boldsymbol{u}^{k-1}\left(\Delta \boldsymbol{u}^{k-1}\right)^T\right)^{-1} \end{cases} \tag{21}$$

$$\boldsymbol{u}^k = \boldsymbol{u}^{k-1} + \rho\left(\lambda \boldsymbol{I} + \left(\hat{\boldsymbol{\Phi}}^k\right)^T \hat{\boldsymbol{\Phi}}^k\right)^{-1}\left(\hat{\boldsymbol{\Phi}}^k\right)^T\left(\boldsymbol{y}_{ref}^{k+1} - \boldsymbol{y}^k\right) \tag{22}$$

where $\hat{\phi}_{ij}^1$ is the initial value of $\hat{\phi}_{ij}^k$; $\lambda>0$, $\mu>0$, $\eta\in(02]$, $\rho\in(01]$; b_1 is a sufficiently small positive number, α is a coefficient related to the system's autocorrelation, while b_2 is a coefficient related to the system's coupling. In the data-driven quantitative multiobjective approach, the algorithm reset mechanism in (21) is introduced to make the PJM estimation algorithm track time-varying parameters faster. The stability of the control algorithm has been demonstrated in [24]. The flowchart of the proposed data-driven quantitative multiobjective control approach is shown in Fig. 6.

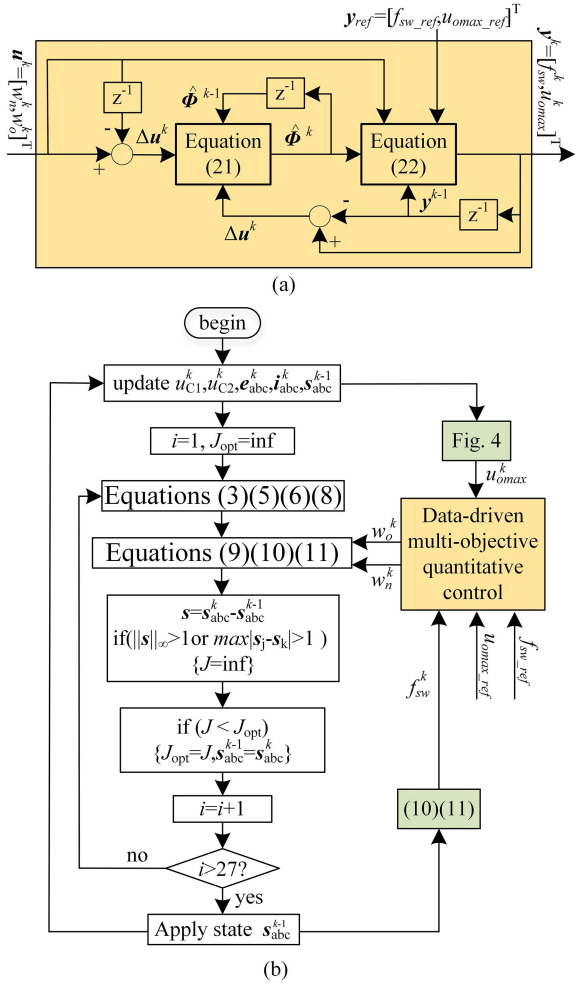

Fig. 6 Principle of proposed data-driven quantitative multiobjective control approach for three-phase three-level NPC inverter. (a) Data-driven quantitative multiobjective control block diagram. (b) System control block diagram.

VI. Simulation and Experimental Results

To verify the validity and superiority of the proposed data-driven quantitative multiobjective control approach for three-phase three-level NPC inverters, we have constructed simulation models and experimental prototypes. The parameters used in the simulations and experiments for the two methods are shown in Table II.

A. Simulation Results

Figs. 7–14 present the simulation results for the proposed data-driven quantitative multiobjective control approach under the conditions of an active power reference $p_{\text{ref}} = 1$pu, a peak deviation of the neutral-point potential within a fixed sliding time window reference $u_{o\max\text{ ref}}$ set at 10 V, and a step change in the switching frequency reference $f_{\text{sw ref}}$ from 600 to 800 Hz. Fig. 7 illustrates the switching frequency response, while Fig. 8 depicts the neutral-point potential response. It is evident that the switching frequency effectively tracks the reference value, and although the neutral-point potential experiences some fluctuations during the transient phase, it quickly stabilizes thereafter.

TABLE II
Main Parameters of the Simulation and Experimental Setup

Parameters	value
Filter inductor L	3.3mH
Filter losses R	0.1Ω
DC-link capacitance C	2200μF*2
Grid-voltage (rms)	90V
Grid frequency	50Hz
Rated dc-link voltage u_{dc}	160V
Reactive power reference q^*	0
per-unit base values for voltage	75V
per-unit base values for current	25A
per-unit base values for frequency	50Hz
Switching frequency sliding window time T_w	20ms
Midpoint potential sliding *window time* T_{lw}	102.4ms
Sampling time T_s	100μs
Step-size factor for the midpoint potential weighting: ξ_{so}	0.0005pu
Step-size factor for the switching frequency: ξ_{sw}	1pu
Sliding window switching frequency weighting factor: w_{sn}	0.1pu
Penalize excessive changes in the control input: λ	100pu
Penalize excessive variations in the estimated PJM: μ	10pu
Step-size factor of input: ρ	0.0075pu
Search step-size of PJM: η	0.1pu

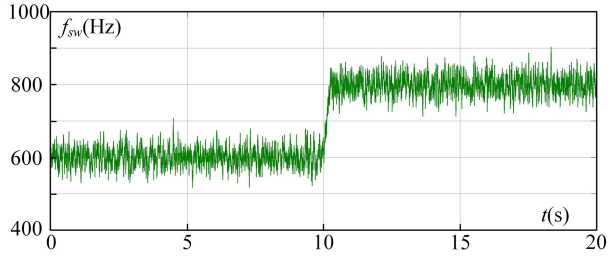

Fig. 7 Simulation waveform of the switching frequency under variable reference switching frequency conditions using the data-driven quantitative multiobjective control approach.

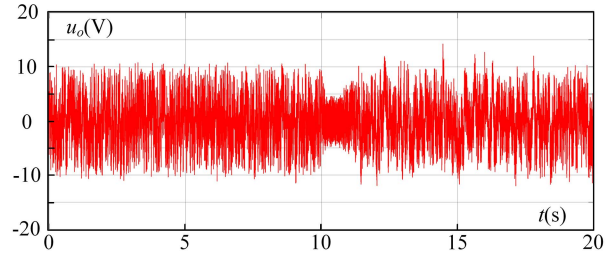

Fig. 8 Simulation waveform of the neutral-point potential under variable reference switching frequency conditions using the data-driven quantitative multiobjective control approach.

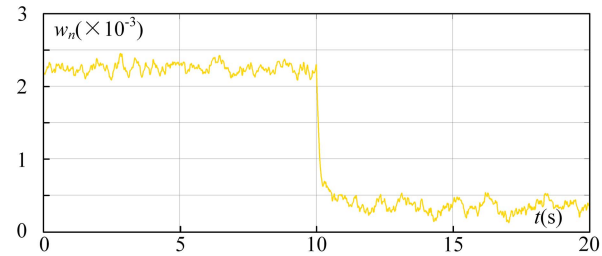

Fig. 9 Simulation waveform of the switching weighting factor under variable reference switching frequency conditions using the data-driven quantitative multiobjective control approach.

Figs. 9 and 10 display the simulation results for the switching weighting factor and the neutral-point potential weighting factor, respectively. When the switching frequency reference values change, the weighting factors automatically adjust to achieve quantitative control of the variables. Figs. 11 and 12 show the phase voltage and three-phase current waveforms of switching frequency at 600 Hz, whereas Figs. 13 and 14 present the corresponding waveforms at 800 Hz. The results indicate that the switching frequency change is accurately reflected, and the current quality is correspondingly altered, which is consistent with the general behavior of conventional FCS-MPC.

These findings collectively demonstrate the effectiveness of the proposed quantitative multiobjective control approach in tracking reference values and maintaining system stability under dynamic conditions.

Figs. 15–20 present the simulation results for the sliding window weighting factor approach under the conditions of an active

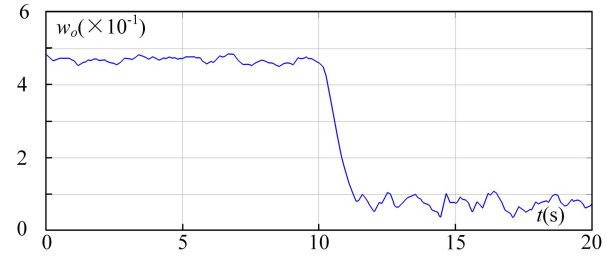

Fig. 10 Simulation waveform of the neutral point potential weighting factor under variable reference switching frequency conditions using the data-driven quantitative multiobjective control approach.

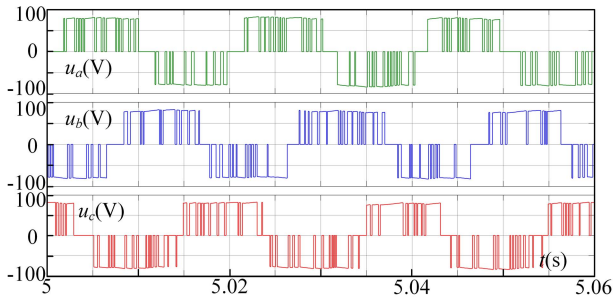

Fig. 11 Simulation waveform of the three-phase voltage with a switching frequency reference value of 600 Hz using the data-driven quantitative multiobjective control approach.

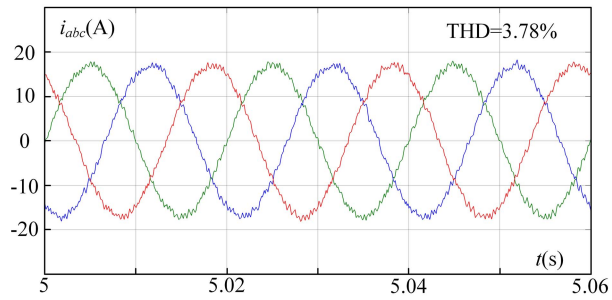

Fig. 12 Simulation waveform of the three-phase current with a switching frequency reference value of 600 Hz using the data-driven quantitative multiobjective control approach.

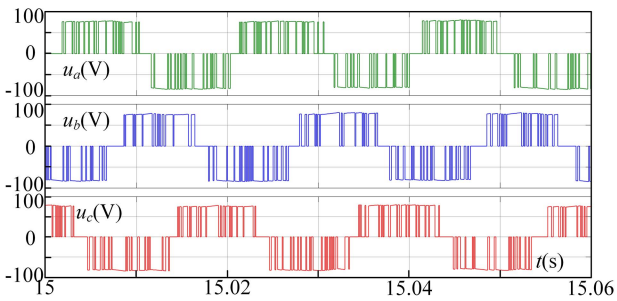

Fig. 13 Simulation waveform of the three-phase voltage with a switching frequency reference value of 800 Hz using the data-driven quantitative multiobjective control approach.

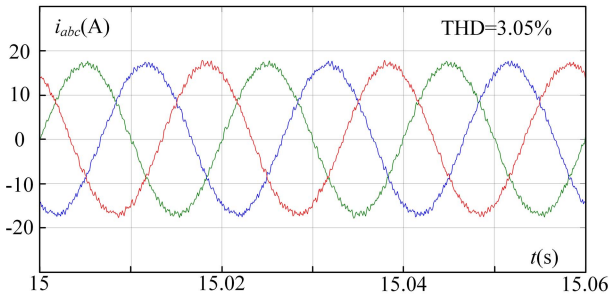

Fig. 14 Simulation waveform of the three-phase current with a switching frequency reference value of 800 Hz using the data-driven quantitative multiobjective control approach.

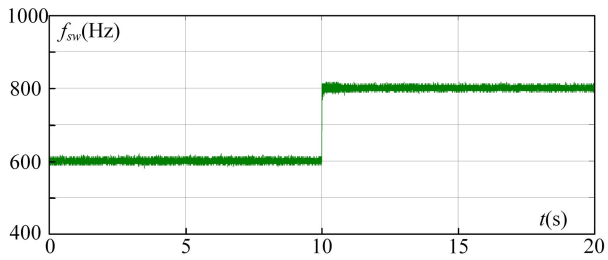

Fig. 15 Simulation waveform of the switching frequency under variable reference switching frequency conditions using the sliding window weighting approach.

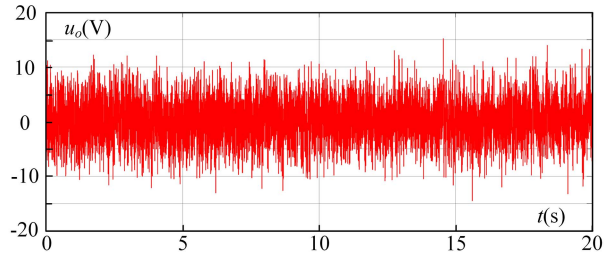

Fig. 16 Simulation waveform of the neutral-point potential under variable reference switching frequency conditions using the sliding window weighting approach.

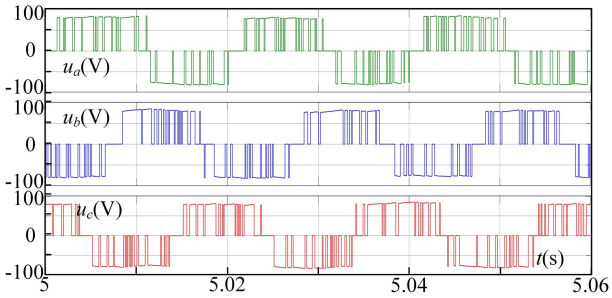

Fig. 17 Simulation waveform of the three-phase voltage with a switching frequency reference value of 600 Hz using the sliding window weighting approach.

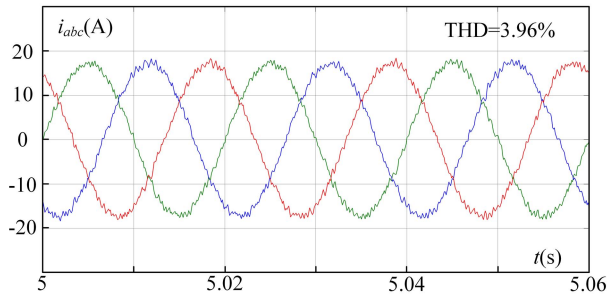

Fig. 18 Simulation waveform of the three-phase current with a switching frequency reference value of 600 Hz using the sliding window weighting approach.

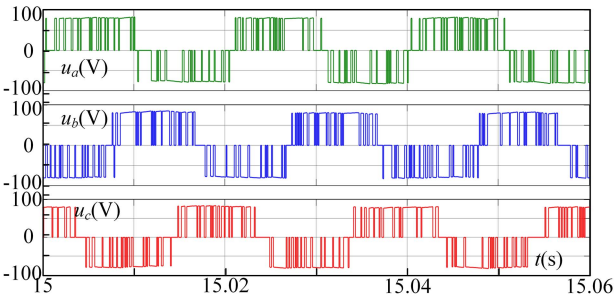

Fig. 19 Simulation waveform of the three-phase voltage with a switching frequency reference value of 800 Hz using the sliding window weighting approach.

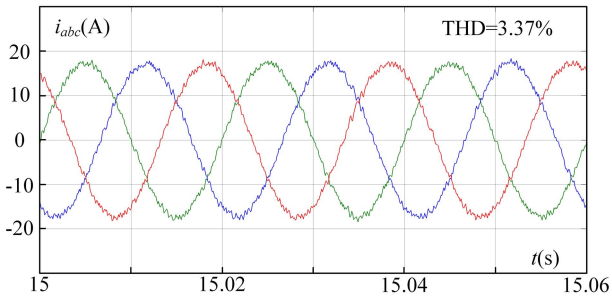

Fig. 20 Simulation waveform of the three-phase current with a switching frequency reference value of 800 Hz using the sliding window weighting approach.

power reference $p_{\mathrm{ref}} = 1$pu, a peak deviation of the neutral-point potential within a fixed sliding time window reference $u_{o\max\,\mathrm{ref}}$ set at 10 V, and a step change in the switching frequency reference $f_{\mathrm{sw\,ref}}$ from 600 to 800 Hz. Fig. 15 illustrates the switching frequency response, while Fig. 16 depicts the neutral-point potential response. Figs. 17 and 18 show the phase voltage and three-phase current waveforms at a switching frequency of 600 Hz, whereas Figs. 19 and 20 present the corresponding waveforms at 800 Hz.

In comparison of the two approaches, the sliding window weighting factor approach exhibits superior performance in terms of switching frequency control. However, the data-driven quantitative multiobjective control approach outperforms the

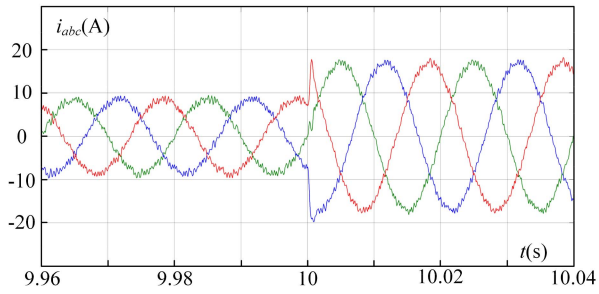

Fig. 21 Simulation waveforms of the three-phase currents under load variation conditions using the data-driven quantitative multiobjective control approach.

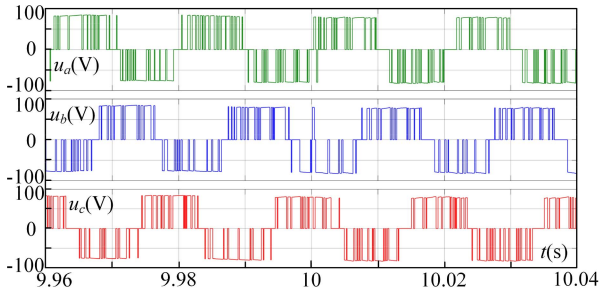

Fig. 22 Simulation waveforms of the phase voltages under load variation conditions using the data-driven quantitative multiobjective control approach.

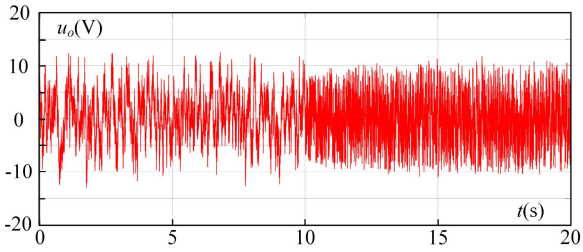

Fig. 23 Simulation waveforms of the neutral-point potential under load variation conditions using the data-driven quantitative multiobjective control approach.

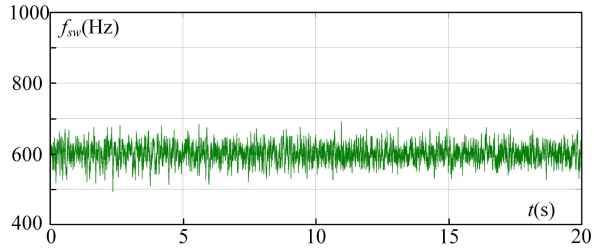

Fig. 24 Simulation waveforms of the switching frequency under load variation conditions using the data-driven quantitative multiobjective control approach.

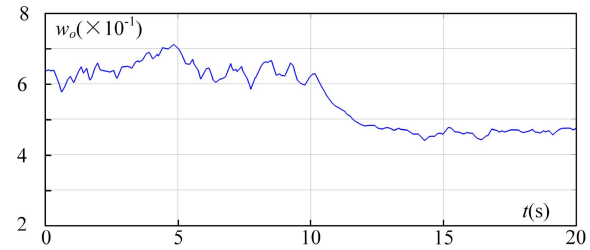

Fig. 25 Simulation waveforms of the neutral point potential weighting factor under load variation conditions using the data-driven quantitative multiobjective control approach.

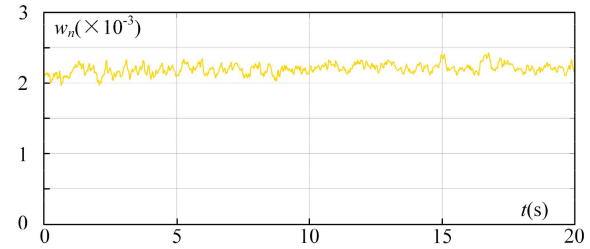

Fig. 26 Simulation waveforms of the switching weighting factor under load variation conditions using the data-driven quantitative multiobjective control approach.

sliding window weighting factor approach in both current THD and neutral point potential control. It should be noted that the value function of the data-driven quantitative multiobjective control approach is consistent with that of the conventional FCS-MPC approach. The objective of the switching frequency optimization term is to reduce the switching frequency. In contrast, the objective of the switching frequency optimization term in the sliding window weighting factor approach is the "regularity of the switching frequency." This difference leads to a tradeoff where other metrics are sacrificed in favor of switching regularity rather than a reduction in switching frequency.

Figs. 21–26 present the simulation results of the proposed data-driven quantitative multiobjective control approach under the conditions of a switching frequency reference $f_{\mathrm{sw\cdot ref}} = 600$ Hz, a neutral point potential reference $u_{o\cdot\mathrm{ref}} = 10$ V, and a step change in the active power reference p_{ref} from 0.5 to 1pu. Figs. 21 and 22 show the waveforms of the three-phase currents and phase voltages, respectively, highlighting the rapid dynamic response of the system to the load change. Figs. 23 and 24 depict the waveforms of the neutral-point potential and switching frequency, respectively, illustrating that the controlled variables still achieve quantitative control even when the load changes. Figs. 25 and 26 display the simulation results for the neutral-point potential weighting factor and the switching weighting factor, respectively. When the load changes, the weighting factors automatically adjust to achieve quantitative control of the variables.

These results collectively demonstrate the effectiveness of the proposed quantitative multiobjective approach in maintaining system stability and achieving quantitative control of the variables under load transient conditions.

Figs. 27–30 present the simulation results of the sliding window weighting factor approach under the conditions of a switching frequency reference $f_{\mathrm{sw\cdot ref}} = 600$ Hz, a neutral point potential reference $u_{o\cdot\mathrm{ref}} = 10$V, and a step change in the active power reference p_{ref} from 0.5 to 1 pu. Figs. 27 and 28 show

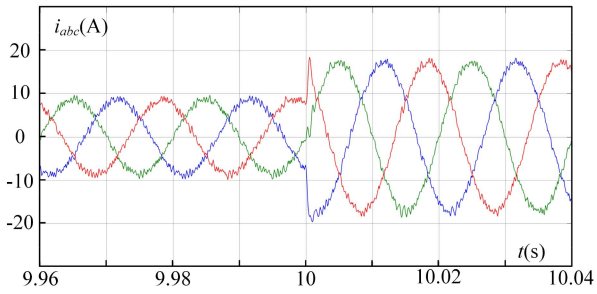

Fig. 27 Simulation waveforms of the three-phase currents under load variation conditions using the sliding window weighting approach.

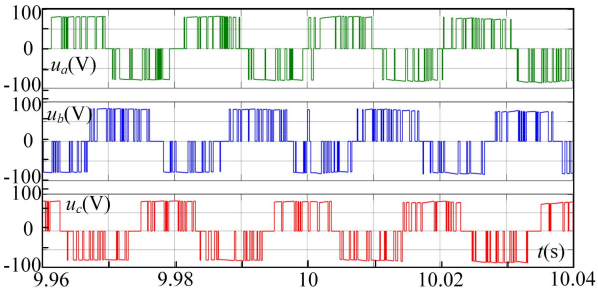

Fig. 28 Simulation waveforms of the phase voltages under load variation conditions using the sliding window weighting approach.

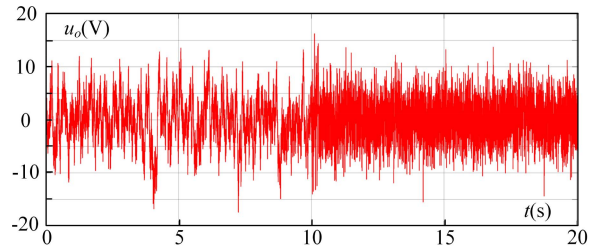

Fig. 29 Simulation waveforms of the neutral-point potential under load variation conditions using the sliding window weighting approach.

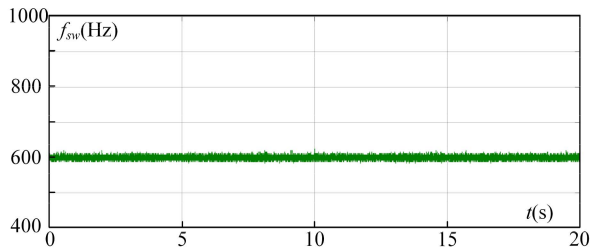

Fig. 30 Simulation waveforms of the switching frequency under load variation conditions using the sliding window weighting approach.

the waveforms of the three-phase currents and phase voltages, respectively, highlighting the rapid dynamic response of the system to the load change. Figs. 23 and 24 depict the waveforms of the neutral-point potential and switching frequency, respectively, illustrating that the controlled variables still achieve quantitative control even when the load changes.

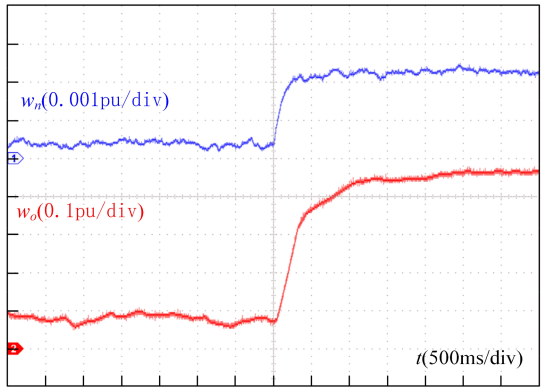

Fig. 31 Experimental waveforms of the switching frequency weighting factor and neutral point potential weighting factor under variable reference switching frequency conditions using the data-driven quantitative multiobjective control approach.

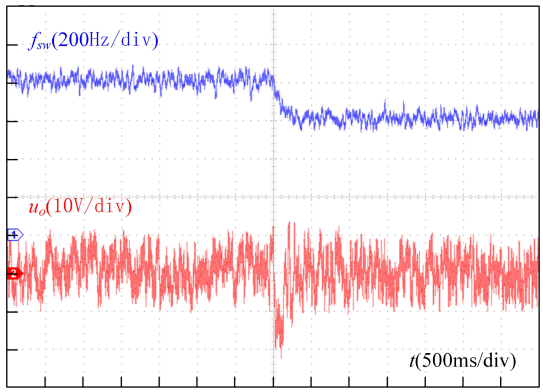

Fig. 32 Experimental waveforms of the switching frequency and neutral-point potential under variable reference switching frequency conditions using the data-driven quantitative multiobjective control approach.

In the comparison of the two approaches, there is no significant difference in the dynamic response of the current. However, the proposed data-driven quantitative multiobjective control approach outperforms the sliding window weighting factor approach in terms of neutral-point potential control.

B. Experiment Results

The proposed data-driven quantitative multiobjective control approach and sliding window weighting factor approach are experimentally validated using a setup with a 300-MIPS 32-bit TMS320C28346 DSP board and IGBTs. The specific experimental parameters are detailed in Table II.

Figs. 31 and 32 present the experimental results for the proposed data-driven quantitative multiobjective control approach under the conditions of an active power reference $p_{\mathrm{ref}} = 1$pu, a peak deviation of the neutral-point potential within a fixed sliding time window reference $u_{o\cdot\mathrm{ref}}$ set at 10V, and a step change in the switching frequency reference $f_{sw\cdot ref}$ from 800 to 600 Hz. The results indicate that when the reference values change, the switching weighting factor and the neutral-point

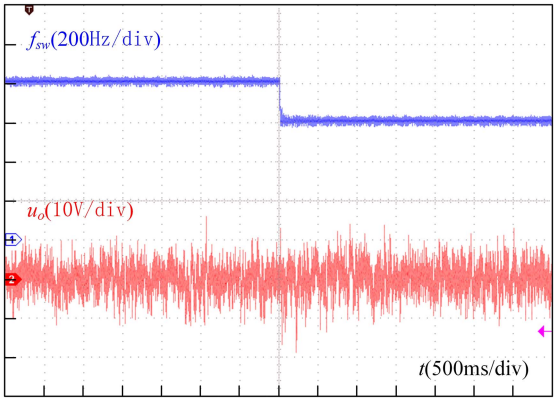

Fig. 33 Experimental waveforms of the switching frequency and neutral-point potential under variable reference switching frequency conditions using the sliding window weighting approach.

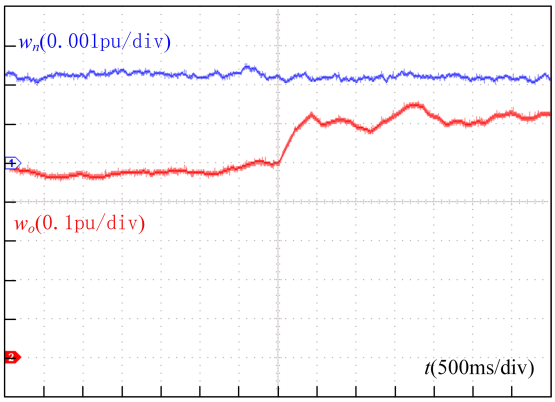

Fig. 34 Experimental waveforms of the switching frequency weighting factor and neutral point potential weighting factor under load variation conditions using the data-driven quantitative multiobjective control approach.

potential weighting factor automatically adjust to achieve quantitative control of the switching frequency and the neutral-point potential. Fig. 33 present the experimental results for the sliding window weighting approach under the conditions of an active power reference $p_{\mathrm{ref}} = 1$pu, a neutral-point potential reference $u_{o\,\mathrm{ref}}$ set at 10 V, and a step change in the switching frequency reference $f_{sw\,\mathrm{ref}}$ from 800 to 600 Hz. It is evident that the constraint on the switching frequency is more stringent in this case.

Figs. 34–36 present the experimental results of the proposed data-driven quantitative multiobjective control approach under the conditions of a switching frequency reference $f_{\mathrm{sw}\,\mathrm{ref}} =$ 600 Hz, a peak deviation of the neutral-point potential within a fixed sliding time window reference $u_{o\,\mathrm{ref}} = 10$V, and a step change in the active power reference p_{ref} from 1 to 0.5 pu. The results indicate that when the load changes, the switching weighting factor and the neutral-point potential weighting factor automatically adjust to achieve quantitative control of the switching frequency and the neutral-point potential.

Figs. 37–38 present the experimental results of the sliding window weighting approach under the conditions of a switching frequency reference $f_{sw\,\mathrm{ref}} = 600$ Hz, a peak deviation of the neutral-point potential within a fixed sliding time window

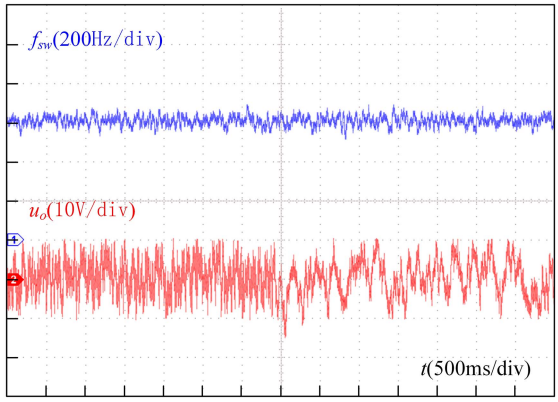

Fig. 35 Experimental waveforms of the switching frequency and neutral-point potential under load variation conditions using the data-driven quantitative multiobjective control approach.

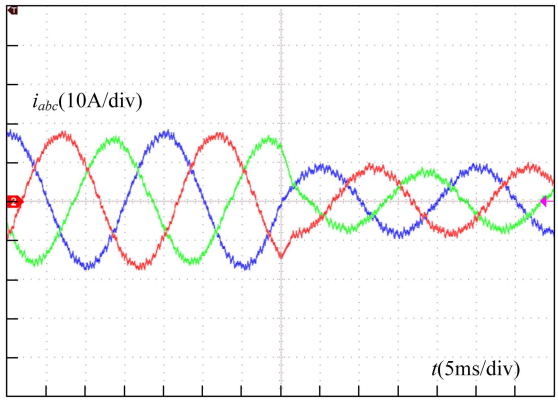

Fig. 36 Experimental waveforms of the three-phase currents under load variation conditions using the data-driven quantitative multiobjective control approach.

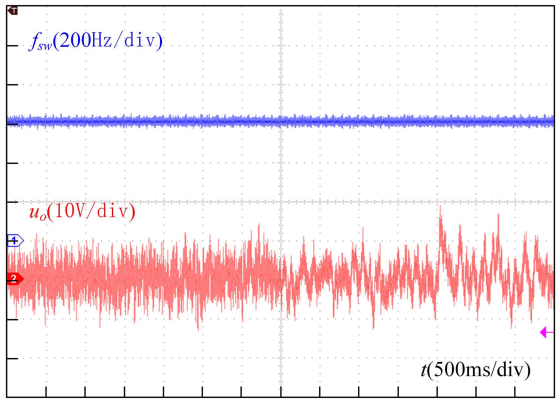

Fig. 37 Experimental waveforms of the switching frequency and neutral-point potential under load variation conditions using the sliding window weighting approach.

reference $u_{o\,\mathrm{ref}} = 10$V, and a step change in the active power reference p_{ref} from 1 to 0.5 pu. It can be discerned that the two methods exhibit no significant disparity in terms of dynamic performance. The sliding window weighting approach exerts more stringent constraints on the switching frequency, thereby

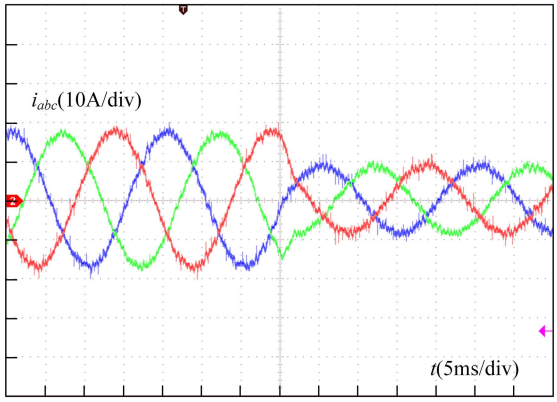

Fig. 38 Experimental waveforms of the three-phase currents under load variation conditions using the sliding window weighting approach.

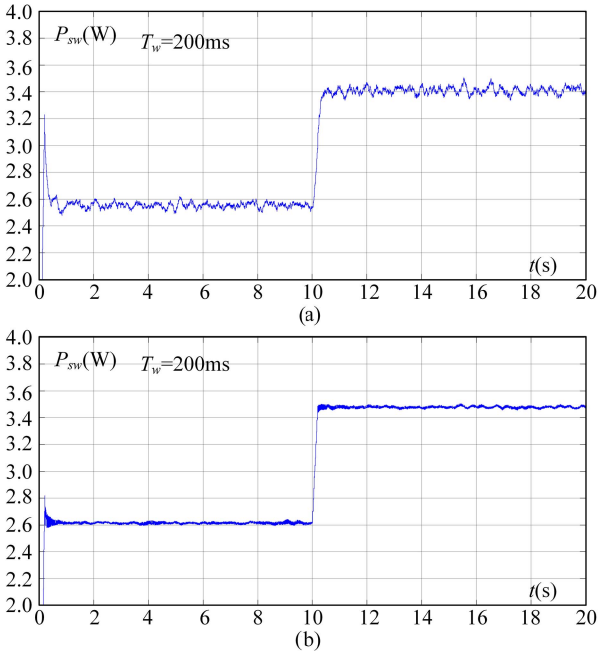

Fig. 39 Calculation results of switching loss power. (a) Data-driven quantitative multiobjective control approach. (b) Sliding window weighting approach.

resulting in the deterioration of control over objectives such as the neutral-point potential.

C. Discussion

The power losses of switching devices primarily consist of conduction losses and switching losses. Under identical operating conditions, conduction losses remain nearly the same across different control strategies; therefore, switching losses constitute the dominant factor influencing overall device power dissipation. Fig. 39 illustrates the switching-loss power waveforms of the two methods when the active power is set to 1 pu, the neutral-point voltage reference is 10 V, and the switching-frequency reference is abruptly changed from 600 to 800 Hz at t = 10 s. It can be observed that, for the same switching-frequency reference, the proposed method exhibits marginally larger fluctuations in instantaneous switching-loss power, yet its average value is slightly lower.

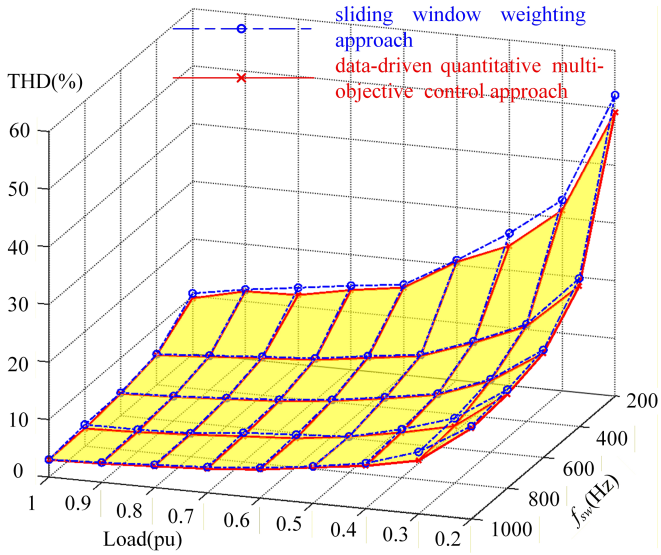

Fig. 40 Current THD results of the two approaches under different load and switching frequency conditions.

To compare the current THD of the two schemes across varying load and switching-frequency conditions, the results are summarized in Fig. 40. As depicted in Fig. 40, under identical load and switching frequency conditions, the data-driven quantitative multiobjective control approach exhibits a lower current THD. This can be attributed to the fact that the value function of the data-driven method is consistent with that of the conventional FCS-MPC, which specifically targets the reduction of switching frequency as its optimization objective.

Conversely, the sliding-window weighting factor approach aims to optimize the average switching frequency within a fixed sliding-window duration, emphasizing the "regularity of switching." This approach ensures that the occurrence of switch actions remains consistent with previous switch actions within the sliding-window period, rather than focusing on the conventional objective of reducing switching frequency. While the sliding-window weighting factor approach demonstrates smaller fluctuations in switching frequency, both methods achieve zero steady-state error in average switching frequency control, leading to comparable switching losses.

Furthermore, the sliding-window weighting factor approach controls switching frequency and neutral-point potential control in a relatively independent manner, without accounting for the coupling between these control objectives. This results in a less effective neutral-point potential control performance. These factors collectively highlight the superior performance of the data-driven quantitative multiobjective control approach.

VII. Conclusion

This article proposes an online self-tuning method for weighting factors within the FCS-MPC framework, achieving quantitative control of multiobjective. The proposed approach has been experimentally verified on a three-phase three-level NPC

inverter, and the results have demonstrated its effectiveness and superiority. The proposed approach provides significant reference for achieving quantitative control of multiobjective in FCS-MPC for other power electronic topologies.

REFERENCES

[1] X. Zhang, Z. Ma, X. Wu, Y. Han, X. Cai, and G. Lin, "Improved model-free predictive current control with forgetting factor," *IEEE Trans. Ind. Electron.*, vol. 72, no. 12, pp. 14949–14953, Dec. 2025, doi: 10.1109/TIE.2025.3569963.

[2] D. Lv, W. Ding, Y. Wang, K. Wang, S. Chen, and J. Cai, "Finite control set model predictive torque control of switched reluctance motor based on three-phase four-leg inverter," *IEEE Trans. Ind. Electron.*, vol. 72, no. 10, pp. 9931–9941, Oct. 2025, doi: 10.1109/TIE.2025.3553184.

[3] X. Zhang, X. Wu, G. Tan, W. Zhang, and Q. Wang, "A dual-vector model predictive control method with minimum current THD," *IEEE Trans. Power Electron.*, vol. 36, no. 9, pp. 9758–9762, Sep. 2021, doi: 10.1109/TPEL.2021.3065009.

[4] X. Zhang et al., "Single-phase three-level PWM rectifier predictive control with fixed switching frequency based on current convex optimization," *IEEE Trans. Power Electron.*, vol. 36, no. 10, pp. 12090–12101, Oct. 2021, doi: 10.1109/TPEL.2021.3073532.

[5] X. Liu, L. Qiu, Y. Fang, K. Wang, Y. Li, and J. Rodríguez, "Event-driven based reinforcement learning predictive controller design for three-phase NPC converters using online approximators," *IEEE Trans. Power Electron.*, vol. 40, no. 4, pp. 4914–4926, Apr. 2025, doi: 10.1109/TPEL.2024.3510731.

[6] X. Zhang, Z. Ma, X. Wu, Y. Han, X. Cai, and G. Lin, "Improved model-free predictive current control with forgetting factor," *IEEE Trans. Ind. Electron.*, vol. 72, no. 12, pp. 14949–14953, Dec. 2025, doi: 10.1109/TIE.2025.3569963.

[7] N. Li, H. Yu, S. Finney, and P. D. Judge, "Long-horizon FCS-MPC trained 1-D convolution neural networks for FPGA-based power-electronic converter control with a Si/SiC hybrid converter case study," *IEEE Trans. Ind. Electron.*, vol. 72, no. 9, pp. 9486–9496, Sep. 2025, doi: 10.1109/TIE.2025.3536555.

[8] X. Zhang, G. Tan, T. Xia, Q. Wang, and X. Wu, "Optimized switching finite control set model predictive control of NPC single-phase three-level rectifiers," *IEEE Trans. Power Electron.*, vol. 35, no. 10, pp. 10097–10108, Oct. 2020, doi: 10.1109/TPEL.2020.2978185.

[9] J. Holtz, "Advanced PWM and Predictive control—An overview," *IEEE Trans. Ind. Electron.*, vol. 63, no. 6, pp. 3837–3844, Jun. 2016, doi: 10.1109/TIE.2015.2504347.

[10] X. Zhang, Z. Ma, X. Cai, X. Wu, Y. Han, and G. Lin, "Enhanced accuracy finite-control-set model-predictive control for three-phase three-level NPC inverter," *IEEE Trans. Power Electron.*, vol. 40, no. 8, pp. 10330–10334, Aug. 2025, doi: 10.1109/TPEL.2025.3551455.

[11] Y. He, Y. Tang, X. Gao, H. Xie, F. Wang, and R. Kennel, "A cascade-free model predictive control scheme for back-to-back converter-fed PMSM drive system," *IEEE Trans. Power Electron.*, vol. 39, no. 4, pp. 4590–4600, Apr. 2024, doi: 10.1109/TPEL.2024.3350897.

[12] Z. Zhang, Z. Zhang, C. Garcia, J. Rodríguez, W. Huang, and R. Kennel, "Discussion on control methods with finite-control-set concept for PMSM drives," in *Proc. IEEE Int. Electric Machines Drives Conf.*, San Diego, CA, USA, 2019, pp. 1718–1723.

[13] S. Xu, C. Yao, G. Ren, Z. Sun, S. Wu, and G. Ma, "Weighting factors autotuning of FCS-MPC for hybrid ANPC inverter in PMSM drives based on deep residual networks," *IEEE Trans. Power Electron.*, vol. 39, no. 12, pp. 16540–16552, Dec. 2024, doi: 10.1109/TPEL.2024.3454250.

[14] F. Wang, F. Cai, D. Huang, Y. Wei, D. Ke, and Z. Zhang, "Multiobjective model predictive control of LCL grid-connected inverter based on an improved gray wolf algorithm," *IEEE Trans. Power Electron.*, vol. 40, no. 9, pp. 13977–13990, Sep. 2025, doi: 10.1109/TPEL.2025.3572213.

[15] J. Hu, J. Zhu, G. Lei, G. Platt, and D. G. Dorrell, "Multi-objective model-predictive control for high-power converters," *IEEE Trans. Energy Convers.*, vol. 28, no. 3, pp. 652–663, Sep. 2013, doi: 10.1109/TEC.2013.2270557.

[16] E. Zerdali, M. Rivera, and P. Wheeler, "A review on weighting factor design of finite control set model predictive control strategies for AC electric drives," *IEEE Trans. Power Electron.*, vol. 39, no. 8, pp. 9967–9981, Aug. 2024, doi: 10.1109/TPEL.2024.3370550.

[17] F. Wang et al., "Design of model predictive control weighting factors for PMSM using Gaussian distribution-based particle swarm optimization," *IEEE Trans. Ind. Electron.*, vol. 69, no. 11, pp. 10935–10946, Nov. 2022, doi: 10.1109/TIE.2021.3120441.

[18] S. Vazquez et al., "An artificial intelligence approach for real-time tuning of weighting factors in FCS-MPC for power converters," *IEEE Trans. Ind. Electron.*, vol. 69, no. 12, pp. 11987–11998, Dec. 2022, doi: 10.1109/TIE.2021.3127046.

[19] O. Machado, P. Martín, F. J. Rodríguez, and E. J. Bueno, "A neural network-based dynamic cost function for the implementation of a predictive current controller," *IEEE Trans. Ind. Inform.*, vol. 13, no. 6, pp. 2946–2955, Dec. 2017, doi: 10.1109/TII.2017.2691461.

[20] X. Liu et al., "Neural predictor-based low switching frequency FCS-MPC for MMC with online weighting factors tuning," *IEEE Trans. Power Electron.*, vol. 37, no. 4, pp. 4065–4079, Apr. 2022, doi: 10.1109/TPEL.2021.3126815.

[21] X. Zhang, Z. Ma, H. Niu, J. Huang, and G. Lin, "Finite-control-set model-predictive control with data-driven switching frequency control for single-phase three-level NPC rectifiers," *IEEE Trans. Ind. Electron.*, vol. 71, no. 7, pp. 7180–7189, Jul. 2024, doi: 10.1109/TIE.2023.3310035.

[22] M. Narimani, B. Wu, V. Yaramasu, Z. Cheng, and N. R. Zargari, "Finite control-set model predictive control (FCS-MPC) of nested neutral point-clamped (NNPC) converter," *IEEE Trans. Power Electron.*, vol. 30, no. 12, pp. 7262–7269, Dec. 2015, doi: 10.1109/TPEL.2015.2396033.

[23] Y. Yang, H. Wen, M. Fan, M. Xie, and R. Chen, "Fast finite-switching-state model predictive control method without weighting factors for T-type three-level three-phase inverters," *IEEE Trans. Ind. Inform.*, vol. 15, no. 3, pp. 1298–1310, Mar. 2019, doi: 10.1109/TII.2018.2815035.

[24] Y. Guo, Z. Hou, S. Liu, and S. Jin, "Data-driven model-free adaptive predictive control for a class of MIMO nonlinear discrete-time systems with stability analysis," *IEEE Access*, vol. 7, pp. 102852–102866, 2019.

[25] Z. Hou and Y. Zhu, "Controller-dynamic-linearization-based model free adaptive control for discrete-time nonlinear systems," *IEEE Trans. Ind. Inform.*, vol. 9, no. 4, pp. 2301–2309, Nov. 2013.

[26] C. A. Rojas, M. Aguirre, S. Kouro, T. Geyer, and E. Gutierrez, "Leakage current mitigation in photovoltaic string inverter using predictive control with fixed average switching frequency," *IEEE Trans. Ind. Electron.*, vol. 64, no. 12, pp. 9344–9354, Dec. 2017.

Xu Zhang received the B.S., M.S., and Ph.D. degrees in electrical engineering from the China University of Mining and Technology, Xuzhou, China, in 2014, 2017, and 2021, respectively.

In 2022, he became a Postdoc with the College of Transportation and National Maglev Transportation Engineering R&D Center, Tongji University, Shanghai, China. His main research interests include model predictive control, multilevel converter, data-driven control, intelligent algorithm, system optimization, and the power supply and drive system of the MAGLEV trains.

Zhixun Ma (Senior Member, IEEE) received the B.S. and M.S. degrees from the China University of Mining and Technology, Xuzhou, China, and the Ph.D. degree from the Technical University of Munich, Germany, in 2006, 2009 and 2014, respectively, all in electrical engineering.

He is currently an Associate Professor of power electronics and electrical drives with National Maglev Transportation Engineering R&D Center, Tongji Univeristy, Shanghai, China. His main research areas include predictive control and sensorless control of electrical drives, renewable energy systems, and FPGA-based digital control of power electronics and drive systems.

Haichuan Niu (Student Member, IEEE) received the B.S. degree in vehicle engineering from the Shanghai University of Engineering Science, Shanghai, China, in 2020, the M.S. degree in transportation engineering in 2023 from Tongji University, Shanghai, China, where he is currently working toward the Ph.D. degree in vehicle electrification and intelligence with the College of Transportation.

His main research interests include multilevel converters, model predictive control, optimized PWM strategy, and ac drives.

Xiang Wu (Member, IEEE) was born in Jiangsu, China, in 1990. He received the B.S. and Ph.D. degrees in electrical engineering and automation from the China University of Mining and Technology, Xuzhou, China, in 2013 and 2019, respectively.

In 2019, he was with the China University of Mining and Technology as a Lecturer of power electronics and electrical drives, where he became an Associate Professor in 2024. He is currently an Associate Professor with the National Maglev Transportation Engineering R&D Center, Tongji University, Shanghai, China. His research interests include traction power supply, advanced control of high-power ac motors for rail transit and sensorless control of ac motors.

Xinbo Cai received the B.S. degree in automation specializing in control theory and engineering and the M.S. degree in control theory and engineering from Shandong University, Jinan, China, in 2004 and 2007, respectively, and the Ph.D. degree in power electronics and electrical engineering from the Institute for Electrical Drive Systems and Power Electronics, Technische Universität München, Munich, Germany, in 2019.

His current research interests include ac drives, high-frequency converters, multilevel converters, and switch-mode power supplies.

Guobin Lin received the M.S. degree in electrical engineering from Southwest Jiaotong University, Chengdu, China, in 1989.

He is currently a Professor and the Deputy Director of the National Maglev Transportation Engineering R&D Center, Tongji University, Shanghai, China. His research interests include maglev vehicle and linear drive research. Prof. Lin has been a Member of the Steering Committee of International Maglev System and Linear Drive Conference since 2014.